Geophysical Journal International

Geophys. J. Int. (2020) **223,** 254–269
Advance Access publication 2020 May 18
GJI Seismology

doi: 10.1093/gji/ggaa231

Tomographic filtering via the generalized inverse: a way to account for seismic data uncertainty

Roman Freissler,[1] Christophe Zaroli,[2] Sophie Lambotte[2] and Bernhard S.A. Schuberth[1]

[1]*Department of Earth and Environmental Sciences, Geophysics Section, Ludwig-Maximilians-Universität München, Theresienstr.* 41, 80333 *München, Germany. E-mail: bernhard@geophysik.uni-muenchen.de*
[2]*Institut de Physique du Globe de Strasbourg, UMR* 7516, *Université de Strasbourg, EOST/CNRS, France*

Accepted 2020 May 4. Received 2019 December 20; in original form 2020 April 28

SUMMARY

Tomographic-geodynamic model comparisons are a key component in studies of the present-day state and evolution of Earth's mantle. To account for the limited seismic resolution, 'tomographic filtering' of the geodynamically predicted mantle structures is a standard processing step in this context. The filtered model provides valuable information on how heterogeneities are smeared and modified in amplitude given the available seismic data and underlying inversion strategy. An important aspect that has so far not been taken into account are the effects of data uncertainties. We present a new method for 'tomographic filtering' in which it is possible to include the effects of random and systematic errors in the seismic measurements and to analyse the associated uncertainties in the tomographic model space. The 'imaged' model is constructed by computing the generalized-inverse projection (GIP) of synthetic data calculated in an earth model of choice. An advantage of this approach is that a reparametrization onto the tomographic grid can be avoided, depending on how the synthetic data are calculated. To demonstrate the viability of the method, we compute traveltimes in an existing mantle circulation model (MCM), add specific realizations of random seismic 'noise' to the synthetic data and apply the generalized inverse operator of a recent Backus–Gilbert-type global *S*-wave tomography. GIP models based on different noise realizations show a significant variability of the shape and amplitude of seismic anomalies. This highlights the importance of interpreting tomographic images in a prudent and cautious manner. Systematic errors, such as event mislocation or imperfect crustal corrections, can be investigated by introducing an additional term to the noise component so that the resulting noise distributions are biased. In contrast to Gaussian zero-mean noise, this leads to a bias in model space; that is, the mean of all GIP realizations also is non-zero. Knowledge of the statistical properties of model uncertainties together with tomographic resolution is crucial for obtaining meaningful estimates of Earth's present-day thermodynamic state. A practicable treatment of error propagation and uncertainty quantification will therefore be increasingly important, especially in view of geodynamic inversions that aim at 'retrodicting' past mantle evolution based on tomographic images.

Key words: Inverse theory; Body waves; Seismic tomography; Structure of the Earth.

1 INTRODUCTION

A fundamental goal of studies of Earth's deep interior is to obtain a quantitative understanding of the buoyancy distribution in the mantle and the forces that drive plate tectonics. This is generally done in two ways: (1) either by trying to first image the present-day mantle structure based on seismic observations, and then to relate the tomographically imaged variations in seismic velocities in one way or the other to the buoyancy distribution and thus to the dynamics of the mantle or (2) by forward-modelling of the evolution of the mantle based on numerical simulations with subsequent assessment of the quality of the model in terms of the present-day buoyancy distribution by comparison of secondary predictions to Earth observations (e.g. seismic body wave traveltimes, full waveforms, geoid undulations, etc.). Oftentimes, such numerical mantle convection models are just compared to tomographic images in terms of correlations and spectral characteristics (e.g. Becker & Boschi 2002; Bull *et al.* 2009; Nakagawa & Tackley 2010).

Over the course of the past decade, tomographic-geodynamic model comparisons have shifted from qualitative comparisons of

the location, morphology and spectral characteristics of seismic structures to quantitative analyses involving the magnitude of the heterogeneities. The morphology of structures in mantle flow models does in fact not so much depend on the internal parameters of the governing equations, but is largely controlled by the surface boundary conditions (which are often taken from plate motion history models). The magnitude of predicted thermal anomalies, on the other hand, is much more fundamentally tied to mantle properties such as its heat budget (e.g. importance of CMB heat flow relative to total heat loss) and viscosity. It has been demonstrated that it is possible to relate the temperature field of a convection simulation to the heterogeneities mapped by seismic tomography in a physically consistent manner allowing for quantitative comparisons (Schuberth *et al.* 2009a). Two aspects are crucial in such comparisons: (1) the temperature-seismic velocity relation needs to properly account for the inherent non-linearities (e.g. by using thermodynamically self-consistent mineralogical models) and (2) the geodynamic models have to be looked at through tomographic lenses; that is, they have to be modified to reflect the effects of uneven data coverage and regularization inherent to the respective tomographic model. Regularization is required to eliminate the non-uniqueness of the tomographic solutions, and the recovered heterogeneity generally is a low-fidelity version of the true structure. In particular norm damping often results in low amplitudes and small average heterogeneity. In global models, the limited resolving power of the tomographic inversions can easily lead to average amplitude differences between true and recovered heterogeneity by a factor of 2 (Schuberth *et al.* 2009a).

A good quantitative understanding of the damping effects and related amplitude reductions in a given tomographic model is important, as geodynamic studies are moving away from forward simulations, starting from an unknown initial condition at some time in the geological past, to so-called retrodictions, in which geodynamic adjoint simulations are used to iteratively optimize for the initial condition based on an assumed known 'terminal' state of the mantle (e.g. Bunge *et al.* 2003; Horbach *et al.* 2014; Colli *et al.* 2018). The present-day thermodynamic state of the mantle in such applications is estimated from one of the existing tomographic models (together with information from mineral physics). Estimates of the terminal state, however, are only meaningful, if the magnitudes of the seismic heterogeneities are correctly transformed into buoyancy variations; that is, if the amplitude reduction introduced through the regularization could somehow be accounted, and at best, corrected for.

A useful tool to mimic the seismological lens is the so-called 'tomographic filtering' of geodynamic models using the resolution operator associated with the tomographic inversion of interest (e.g. Mégnin *et al.* 1997; Ritsema *et al.* 2007; Bull *et al.* 2009; Schuberth *et al.* 2009a; Davies *et al.* 2012; Koelemeijer *et al.* 2018; Simmons *et al.* 2019). The estimated model filtered in this way provides valuable information on how true Earth structure might actually be seen through tomographic lenses and how heterogeneities are smeared and modified in amplitude. Although explicit knowledge of the resolution operator, typically denoted $\mathcal{R}$, is required for this technique, as well as for the appraisal of a tomography's underlying local resolution, only few authors have fully computed it (by using some approximations or using efficient computational strategies; e.g. Boschi 2003; Soldati *et al.* 2006; Ritsema *et al.* 2007, 2011; Koelemeijer *et al.* 2015; Bogiatzis *et al.* 2016). Calculating the resolution operator is computationally very intense (if not prohibitive for large problems), since a complete tomographic inversion must be performed for each of the model parameters (considering that some modern tomographic inversions try to constrain more than a million free parameters). Recently, Simmons *et al.* (2019) demonstrated that even for very large inversions, $\mathcal{R}$ can still be approximated using a 'multiple impulse response method'.

While typical tomographic filtering using $\mathcal{R}$ allows to mimic the effects of inhomogeneous data coverage and smearing, another reason for a filtered model to be different from the true model is the presence of noise in the seismic data. Like any observation, seismic data are associated with errors and measurement uncertainties (e.g. Gudmundsson *et al.* 1990; Bolton & Masters 2001) that can propagate as 'noise' into the model solution during the inversion process. Thus, the full appraisal of any resulting tomographic image involves the analysis of both the resolution as well as the uncertainties arising from propagated noise. Throughout the paper, the term 'model uncertainty' is used restrictively in the sense that it describes only the effect of propagated noise and we make a clear distinction between uncertainty and resolution, which also is a source of error in the model solution. Most important, uncertainties in model parameters have not yet been taken into account for the tomographic filtering of geodynamic models. This has mainly two reasons: On the one hand, filtering with $\mathcal{R}$ cannot account for model uncertainties through propagated noise because it merely describes the mapping of a single 'true' model to its filtered version. On the other hand, most global tomographies lack an explicit inspection of their uncertainties because the large matrices required to evaluate the model covariance are computationally difficult to deal with (e.g. Nolet 2008).

Recently, Zaroli (2016) introduced the SOLA formulation of linear Backus–Gilbert (B–G) inversions for global seismic tomography that has several relevant advantages compared to a classical damped-least squares (DLS) inversion (Zaroli *et al.* 2017): (1) SOLA B–G directly computes the generalized inverse operator $\mathbf{G}^{\dagger}$ of a given tomographic experiment while enabling an actual control and straightforward quantification of model resolution and model uncertainties, which is in practice often not possible with DLS for global-scale applications; (2) SOLA B–G may be computationally more efficient than DLS, because it allows for embarrassingly parallel computations of the general solution to the inverse problem; (3) there is no need of introducing any constraints on the model values such as through damping in DLS for eliminating the non-uniqueness of the problem (which does not imply that there is no kind of regularization necessary in SOLA B–G, see Section 2.2.2) and (4) The resolution operator $\mathcal{R}$ can be constructed such that the model is an unbiased localized average of the true parameters, which is not necessarily fulfilled in DLS models. In other words, although the SOLA B–G inversion may provide a blurred and distorted image of the structures, each model parameter is—by design—the true average over the local resolving volume. In particular in light of estimating the buoyancy distribution from tomographic models in geodynamic applications, this is of great importance. It means that—given appropriate conversion of seismic velocity to density—the mass would be 'conserved' locally within the resolving volume through the unbiased averaging. The averaging volume itself is explicitly known *a posteriori*; that is, it is clear over which region buoyancy forces have been integrated in the inversion process. The SOLA B–G framework thus bears a large potential for linking seismic data to geodynamic models in a quantitative way.

Considering these features of SOLA B–G tomography, we will show how to incorporate model uncertainties in the tomographic filtering of geodynamic models in the context of such inversions. We first review classical tomographic filtering using $\mathcal{R}$ from SOLA B–G and apply it to the geodynamic model of Nerlich *et al.* (2016). For

convenience, we shall make use of the first SOLA B–G tomographic model from Zaroli (2016), hereafter simply called *SOLA-Z16*. The data that was used for SOLA-Z16 is a subset of the data used in Zaroli *et al.* (2015) and comprises 79 765 finite-frequency delay times measured at 22 s period for *S* and *SS* waves. With these measurements, SOLA-Z16 covers the depth range from 400 to 1710 km. Having computed a 'classical' tomographically filtered model, we then illustrate how to obtain filtered images of the geodynamic model that are able to account for noise in the seismic data, which we call generalized-inverse projection (GIP). We particularly focus on demonstrating that propagating noise has a considerable effect, which can not be ignored for quantitatively linking geodynamic to tomographic models. More specifically, we systematically investigate how different noise realizations are mapped into model space. We start this analysis with treating the uncertainty of each datum with Gaussian noise statistics of varying magnitude, which gives rise to model uncertainty that is equivalent to the model variance estimated directly in the SOLA B–G framework. We then illustrate the effects of potential biases in the noise statistics, such as, for example, systematic errors due to modelling assumptions, uncertainties in event parameters or those related to crustal corrections, among others. Here, we study the effects resulting from the imperfect knowledge of crustal structure as one example. A bias in the noise statistics is introduced through the difference between two published crustal models. As we will show, the mean effect on model parameters no longer is zero in case of biased noise.

2 TOMOGRAPHIC FILTERING

2.1 Preamble

The basic forward problem of linear seismic tomography can be written as

$$\mathbf{d} = \mathbf{G}\mathbf{m} \;\; (+\,\text{noise})\,, \tag{1}$$

where $\mathbf{d}$ is the data of size N, $\mathbf{m}$ the 'true' model parameters of size M and $\mathbf{G}$ the sensitivity matrix of size $N \times M$; that is, a linear operator mapping the model parameters to the data space. In this study, each row of the sensitivity matrix $\mathbf{G}$ represents a finite-frequency S-wave sensitivity kernel projected onto the tomographic grid, but it could also be ray-theoretical sensitivities or similar. The data vector $\mathbf{d}$ thus represents a set of traveltime residuals, while the entries of the true-model vector $\mathbf{m}$ are S-wave velocity perturbations (note that we shall further elaborate on the data noise in Section 3). The solution to the corresponding inverse problem is a model estimate $\tilde{\mathbf{m}}$, which can be expressed as a linear combination of the data

$$\tilde{\mathbf{m}} = \mathbf{G}^{\dagger}\mathbf{d}\,, \tag{2}$$

with the matrix $\mathbf{G}^{\dagger}$ being *some* generalized inverse of $\mathbf{G}$. We obtain the main equation of tomographic filtering by combining eqs (1) and (2) to get

$$\tilde{\mathbf{m}} = \mathcal{R}\mathbf{m} \;\; (+\,\text{propagated noise})\,, \tag{3}$$

where the resolution operator $\mathcal{R}$ is defined as $\mathcal{R} = \mathbf{G}^{\dagger}\mathbf{G}$. The term $\mathcal{R}\mathbf{m}$ is commonly referred to as the 'tomographically filtered' version of the true model. The true model can in general be any kind of 'synthetic' model, but in tomographic-geodynamic model comparisons usually is taken to be the resulting present-day state of a mantle convection simulation.

To calculate the tomographically filtered image of a 'true' model $\mathbf{m}$, directly calculating $\mathcal{R}\mathbf{m}$ is only possible if the model is given in the parametrization defined by the associated tomographic grid. In our case, for example, the SOLA-Z16 tomographic model is irregularly locally parametrized with about 40,000 cells. Since geodynamic models generally are based on rather different parametrizations with many more parameters (nowadays with up to 10^8 grid nodes), one first has to perform a reparametrization onto the tomographic grid.

As $\mathcal{R}$ does not contain information on model uncertainties, tomographic-geodynamic model comparisons have so far been left with ignoring the contribution of 'propagated noise' within the tomographic model. Before we introduce the new filtering approach based on the SOLA B–G generalized inverse, we investigate the results of the SOLA B–G tomographic filtering with $\mathcal{R}$. To this end, we start by reviewing how the resolution operator $\mathcal{R}$ is constructed in DLS and SOLA B–G inversion schemes. With this, we want to highlight that $\mathcal{R}$ from SOLA B–G also has some favourable properties that facilitate and improve the usage for tomographic filtering.

2.2 Tomographic resolution operators

2.2.1 The damped least-squares approach

From a least-squares (LS) point of view, the general model solution for the linear inverse problem would be

$$\tilde{\mathbf{m}} = \arg\min_{\mathbf{m}} \;\; (\mathbf{d} - \mathbf{G}\mathbf{m})^T \mathbf{C}_d^{-1} (\mathbf{d} - \mathbf{G}\mathbf{m})\,, \tag{4}$$

where $\mathbf{C}_d$ is the data covariance matrix describing the uncertainty of individual measurements as well as potential intercorrelations. In many practical applications, the data covariance matrix is assumed to be diagonal: $\mathbf{C}_d = \text{diag}(\sigma_{d_i}^2)_{1 \le i \le N}$ (with σ_{d_i} the standard deviation of measurement d_i); that is, the data noise is uncorrelated. Owing to data errors and the ill-conditioning of $\mathbf{G}$, the problem must be 'regularized' in practice (see e.g. Nolet 2008; Voronin & Zaroli 2018). For example, a so-called damping factor Θ can be introduced, leading to the damped least-squares (DLS) minimization problem that can be formulated as follows:

$$\tilde{\mathbf{m}} = \arg\min_{\mathbf{m}} \;\; \underbrace{(\mathbf{d} - \mathbf{G}\mathbf{m})^T \mathbf{C}_d^{-1} (\mathbf{d} - \mathbf{G}\mathbf{m})}_{\substack{\text{data} \\ \text{misfit}}} + \underbrace{\mathbf{m}^T \mathbf{C}_m^{-1} \mathbf{m}}_{\substack{\text{model norm} \\ \text{penalty}}}\,, \tag{5}$$

where for the sake of simplicity the prior model covariance matrix is often chosen in the form: $\mathbf{C}_m = \Theta^{-2}\mathbf{I}_M$, with $\mathbf{I}_M$ the identity matrix of order M. In other words, the main idea of the DLS approach is to mutually minimize the data misfit and a damped L_2-norm of the model. One way to select an appropriate Θ consists in analysing the trade-off curve between the reduced chi-square measure of data misfit and the model norm (e.g. Nolet 2008). This way, it is possible to deal with the problem of non-uniqueness (of the least-squares solution) and construct reasonable global tomographic models. The 'damped least-squares' solution to the inverse problem can therefore be written as

$$\tilde{\mathbf{m}} = \mathbf{G}^{\dagger}\mathbf{d} = \underbrace{(\mathbf{G}^T \mathbf{C}_d^{-1} \mathbf{G} + \mathbf{C}_m^{-1})^{-1} \mathbf{G}^T \mathbf{C}_d^{-1}}_{\substack{\text{generalized} \\ \text{inverse}}} \mathbf{d}\,, \tag{6}$$

where $\mathbf{G}^{\dagger}$ is the DLS generalized inverse matrix. Thus, the DLS resolution matrix can be written as

$$\mathcal{R} = \mathbf{G}^{\dagger}\mathbf{G} = (\mathbf{G}^T \mathbf{C}_d^{-1} \mathbf{G} + \mathbf{C}_m^{-1})^{-1} \mathbf{G}^T \mathbf{C}_d^{-1} \mathbf{G}\,, \tag{7}$$

which clearly depends on Θ through the term $\mathbf{C}_m^{-1}$. A common way to estimate the DLS model solution $\tilde{\mathbf{m}}$ is to use the LSQR method

(Paige & Saunders 1982), which does not require the explicit computation of $\mathbf{G}^{\dagger}$ and thus saves considerable computational efforts when dealing with large problems, such as in this study. For more details, the reader is referred to, for example, Nolet (2008) and Zaroli *et al.* (2017).

The resulting DLS models are damped estimates of the true model, since the DLS generalized inverse $\mathbf{G}^{\dagger}$ depends on the subjective choice of a particular value for Θ. This may lead to filtered models $\mathcal{R}\mathbf{m}$ (and individual model parameter estimates) that are locally biased toward either lower or higher values, especially in regions with poor data coverage. In other words, the quantity $U_k = \sum_{j=1}^{M} \mathcal{R}_{kj}$ may differ from 1 for some model parameter indices k (Nolet 2008), which would represent an averaging bias. An illustration of the consequences of such an averaging bias, which may lead to misinterpretations of tomographic features, is given in Zaroli *et al.* (2017).

2.2.2 *The SOLA Backus–Gilbert approach*

Rather than computing damped model solutions, the linear SOLA Backus–Gilbert inversion scheme aims at seeking unbiased weighted averages of the continuous true-model properties (Backus & Gilbert 1967, 1968, 1970; Pijpers & Thompson 1992; Zaroli 2016; Zaroli *et al.* 2017). In other words, the model parameters $(\hat{m}_k)_{1\leq k\leq M}$ are estimated as

$$\hat{m}_k = \int A^{(k)}(\mathbf{r})\, m(\mathbf{r})\, d^3\mathbf{r} \;\; (+\,\text{propagated noise})\,, \tag{8}$$

where m denotes the continuous true model. For this average $\hat{m}_k$ to be unbiased, the averaging kernel $A^{(k)}$ has to satisfy the 'unimodular condition':

$$\int A^{(k)}(\mathbf{r})\, d^3\mathbf{r} = 1\,. \tag{9}$$

To get fully unbiased averages, these kernels should also be strictly non-negative in order to meet the conventional definition of a weight function, which may not always be honoured, depending on the quality of the available data coverage. The most important aspect concerning the averaging kernels, also sometimes called resolving kernels, is that they may inform us on the local resolution of tomographic images.

In the case of a discretized representation of the physical domain, one rather seeks each model estimate $\hat{m}_k$ as a weighted average over the discrete true-model parameters $(m_j)_{1\leq j\leq M}$, that is:

$$\hat{m}_k = \sum_{j=1}^{M} \mathcal{R}_{kj} m_j \;\; (+\,\text{propagated noise})\,, \tag{10}$$

with the kth row of the resolution matrix $\mathcal{R}$ such that

$$\sum_{j=1}^{M} \mathcal{R}_{kj} = 1\,. \tag{11}$$

We want to give a short review of the relevant quantities and equations of the SOLA B–G tomographic scheme in the following. The tomographic model SOLA-Z16 of Zaroli (2016) is irregularly locally parametrized, with the mantle being vertically subdivided in 18 distinct layers of 100–200 km width and each layer being laterally defined by an irregular spherical Delauney mesh whose spatial distribution is optimized according to ray density (see Fig. 1). This parametrization leads to 38 125 model parameters in total and a minimal lateral resolving length given explicitly by the local grid node spacing (ranging from about 200–1000 km).

In the case of such an irregular, local tomographic grid, let $A_j^{(k)}$ be the jth discretized component of the kth (continuous) averaging kernel $A^{(k)}$, and V_j be the 'volume' associated to the jth parameter. Then, Zaroli (2016) shows that one has the following relation between the averaging kernel components and those of the resolution matrix

$$\mathcal{R}_{kj} = V_j A_j^{(k)}\,. \tag{12}$$

Note that in the case of a local and 'orthonormal' model parametrization (i.e. all V_j constant, say equal to one), one has the relation $\mathcal{R}_{kj} = A_j^{(k)}$, which means that the kth row of the resolution matrix $\mathcal{R}$ represents the kth resolving kernel. For more details concerning the parametrization of the SOLA-Z16 model, the reader is referred to Zaroli (2010, 2016) and Zaroli *et al.* (2015).

In the following, $\mathbf{x}^{(k)}$ can be treated as the kth row of the SOLA B–G generalized inverse matrix $\mathbf{G}^{\dagger}$, where k is an index representing the kth model parameter. The key idea in the SOLA B–G method (Pijpers & Thompson 1992, 1993) is to specify an *a priori* 'target form' for each resolving kernel. That is, one has to specify M target resolving-kernels $T^{(k)}$, hereafter referred to as target kernels for short, such that their spatial extent represents some *a priori* estimate of the spatial resolving-length at each parameter location. The SOLA B–G inversion scheme consists in solving for each vector $\mathbf{x}^{(k)}$ the minimization problem

$$\min_{\mathbf{x}^{(k)}} \; \underbrace{\int \left(A^{(k)} - T^{(k)}\right)^2 d^3\mathbf{r}}_{\substack{\text{resolution}\\ \text{misfit}}} + \eta_k^2 \underbrace{\sigma^2_{\hat{m}_k}}_{\substack{\text{model}\\ \text{variance}}}\,, \;\; \text{s.t. eq. (9)}\,, \tag{13}$$

which can be rewritten in a discrete fashion corresponding to our irregular tomographic grid. The extra condition in eq. (9) is equivalent to $\sum_{j=1}^{M} \mathcal{R}_{kj} = 1$; that is, it enforces the unbiased averaging over the true model parameters. The left-hand term in eq. (13) defines a resolution misfit between the kth averaging (resolving) kernel $A^{(k)}$ and its associated target kernel $T^{(k)}$, whereas the right-hand term reflects the model variance, $\sigma^2_{\hat{m}_k}$, that both get minimized jointly with different weighting given by the trade-off parameter η_k. η_k can be chosen freely to assure a certain balance between model resolution and uncertainties. In other words, by the very formulation of the minimization problem, one has a certain control over those two quantities that are crucial for the appraisal of tomographic models. Although it would be possible to assign at each grid node $\mathbf{r}_k$ a different value η_k, Zaroli (2016) and Zaroli *et al.* (2017) showed that globally coherent tomographic images can be obtained with a constant η for all grid nodes within one layer provided that the size of the target kernels is tuned to the spatially irregular data coverage. This way, it is possible to reduce the number of free tuning parameters in the SOLA B–G inversion scheme and hence to decrease its computational cost. SOLA B–G solutions, like with any inversion scheme, thus depend on tunable parameters, so that different choices would result in different models. Nevertheless, although one can not evade making specific choices for target kernels and trade-off parameters, it is important to note that any particular solution represents unbiased model averages, associated with different resolving volumes, that each can be quantitatively analysed in conjunction with their respective model uncertainties. Put differently, in contrast to the regularization in DLS through damping and/or smoothing that act directly on the model values, the problem of non-uniqueness is in SOLA B–G dealt with by explicitly computing averaging kernels under the unimodular condition in eq. (9) and the constraint on the model variance controlled by the trade-off parameter.

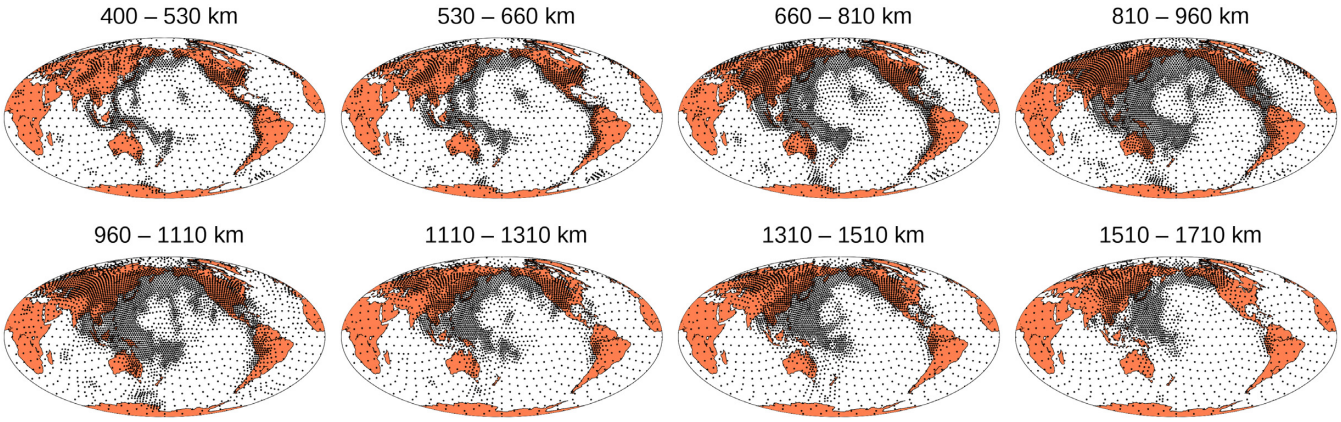

Figure 1. Grid nodes of the SOLA-Z16 tomographic model (Zaroli 2016). The mantle is vertically parametrized by distinct depth layers and laterally by an irregular spherical Delauney mesh that is optimized according to ray density. The SOLA-Z16 model is currently limited to the depth range between 400 and 1710 km owing to the coverage of the specific seismic data used.

Finally, to compute the SOLA B–G generalized inverse $\mathbf{G}^{\dagger}$, respectively its kth row $\mathbf{x}^{(k)}$, Zaroli (2016) showed how to solve the aforementioned minimization problem using the LSQR algorithm (Paige & Saunders 1982). Note that each row of the SOLA B–G generalized inverse (i.e. $\mathbf{x}^{(k)}$) can be computed independently from the others, thus making the SOLA B–G tomographic scheme well suited for (embarrassingly) parallel computations. Once the generalized inverse coefficients $\mathbf{x}^{(k)} = (x_i^{(k)})_{1\leq i\leq N}$ are known, one can directly infer the estimate $\hat{m}_k$, the resolving kernel $A^{(k)}$ (i.e. kth row of resolution matrix $\mathcal{R}$) and the uncertainty $\sigma_{\hat{m}_k}$ as follows:

$$\mathbf{x}^{(k)} \Longrightarrow \begin{cases} \sum_{i=1}^{N} x_i^{(k)} d_i & \longrightarrow \hat{m}_k \\ \sum_{i=1}^{N} x_i^{(k)} G_{ij} & \longrightarrow \mathcal{R}_{kj} \\ (\sum_{i=1}^{N} (x_i^{(k)})^2 (\sigma_{d_i})^2)^{1/2} & \longrightarrow \sigma_{\hat{m}_k}\,. \end{cases} \tag{14}$$

Despite the fact that the SOLA B–G method does not specifically aim at minimizing a data misfit, it has been shown in Zaroli *et al.* (2017) that SOLA models computed from eq. (14) are actually able to fit the corresponding data sets at the same level as DLS models. We verified that this is likewise true for the SOLA-Z16 model used here.

With the nice property of providing uncertainty information alongside with resolution, the linear SOLA B–G tomographic scheme is particularly suited for tomographic filtering and represents a useful tool for more quantitatively comparing tomographic models and geodynamic predictions. Most important, since the full generalized inverse is directly computed in the SOLA B–G approach, the calculation of $\mathcal{R}$ is straightforward and one can easily access the individual model uncertainties ($\sigma_{\hat{m}_k}$)—which represent the propagation of data noise into the model solution—by projecting a large number of noise realizations into model space using $\mathbf{G}^{\dagger}$. We introduce this method in more detail in the following.

2.3 Generalized-inverse projection

As mentioned in the beginning, classic tomographic filtering of synthetic earth models based on $\mathcal{R}\mathbf{m}$ has proven to be an efficient tool for the assessment of geodynamic models. In this regard, the SOLA B–G method provides us now with a resolution operator $\mathcal{R}$ that leads to an *unbiased* filtering of synthetic models—while so far, DLS-based tomographic filtering studies have potentially been suffering from biased-filtering effects—and additionally allows us to perform a quantification of the effects of seismic data noise that propagates into the tomographic solution. In the following, we will illustrate that with the generalized inverse, it is possible, and trivial, to take noise into account. Note that although we base our illustration on the SOLA B–G tomography, this method works for all cases where the generalized inverse can explicitly be computed.

In our study, we consider noise as any error in the traveltime residuals; that is, the random measurement errors, which can only be estimated and described statistically, as well as potentially present systematic errors such as, for example, earthquake mislocation, uncertainties in origin time or effects related to crustal corrections. Let us therefore rewrite eq. (1) by explicitly adding the term that accounts for data uncertainty in form of a vector of seismic noise $\mathbf{n} = (n_i)_{1\leq i\leq N}$, which describes the error affecting the measured traveltime residual data $\mathbf{d}$:

$$\mathbf{d} = \mathbf{G}\mathbf{m} + \mathbf{n}\,. \tag{15}$$

In the SOLA B–G tomographic inversion scheme, each entry of $\mathbf{n}$ is generally assumed to be independent of all others and normally distributed with zero mean and variance $\sigma_{d_i}^2$. In other words, the corresponding data covariance matrix $\mathbf{C}_d$ is assumed to be diagonal, that is: $\mathbf{C}_d = \mathrm{diag}(\sigma_{d_i}^2)_{1\leq i\leq N}$.

In addition to using the new, unbiased, SOLA B–G tomographic resolution operator ($\mathcal{R}$), the main goal of this study is to go beyond the classic comparison of tomographic models with tomographically filtered versions ($\mathcal{R}\mathbf{m}^{\mathrm{syn}}$) of a given synthetic model. Indeed, we believe that it should be more quantitative and robust to compare tomographic models with what we call the GIP versions of the synthetic models, hereafter denoted by $\hat{\mathbf{m}}^{\mathrm{GIP}}$ and defined as

$$\begin{aligned} \hat{\mathbf{m}}^{\mathrm{GIP}} &= \mathbf{G}^{\dagger}\mathbf{d}^{\mathrm{syn}} \\ &= \mathbf{G}^{\dagger}\mathbf{d}^{\mathrm{syn}}_{\mathrm{clean}} + \mathbf{G}^{\dagger}\mathbf{n}^{\mathrm{syn}}\,, \end{aligned} \tag{16}$$

where $\mathbf{d}^{\mathrm{syn}}$ is a synthetic data set, in our study shear-wave traveltime variations, composed of error-free synthetic data generated in the model, $\mathbf{d}^{\mathrm{syn}}_{\mathrm{clean}}$, and some random synthetic noise $\mathbf{n}^{\mathrm{syn}}$ that is generated based on the statistical distribution of the real data noise. To best represent the real-world situation, one should favour computing full 3-D wave fields and full waveform seismograms in the synthetic model to generate the 'clean' data, but this is currently computationally intractable given the large number of earthquakes included in the tomographic data sets. As the tomographic model SOLA-Z16 utilizes finite-frequency kernels, alternatively one could

compute the synthetic data by $\mathbf{d}^{\mathrm{syn}}_{\mathrm{clean}} = \mathbf{G}\mathbf{m}^{\mathrm{syn}}$, which would lead to:

$$\begin{aligned}\hat{\mathbf{m}}^{\mathrm{GIP}} &= \mathbf{G}^{\dagger}\mathbf{G}\mathbf{m}^{\mathrm{syn}} + \mathbf{G}^{\dagger}\mathbf{n}^{\mathrm{syn}} \\ &= \underbrace{\mathcal{R}\mathbf{m}^{\mathrm{syn}}}_{\substack{\text{tomographically}\\ \text{filtered model}}} + \underbrace{\mathbf{G}^{\dagger}\mathbf{n}^{\mathrm{syn}}}_{\substack{\text{propagated}\\ \text{noise}}} . \end{aligned} \tag{17}$$

Formally, GIP models are thus equal to the tomographically filtered synthetic model plus a specific amount of noise propagating into the model solution. Note that the generalized inverse $\mathbf{G}^{\dagger}$ is therefore the key for both the mapping from the true model to the filtered model and the propagation of data errors.

The advantage of the GIP approach is that computing synthetic data, in one way or the other, and projecting it to model space with $\mathbf{G}^{\dagger}$ circumvents the need to reparametrize the model. The effects of reparametrization (i.e. the loss of short-scale heterogeneity) are rather unphysical and may vary with depth (Schuberth *et al.* 2009a), depending on the respective tomographic model. Schuberth *et al.* (2009a) demonstrated that these effects can in an average sense be corrected for when comparing geodynamic and tomographic models on statistical grounds, but it is not clear to what extent such a correction in fact is necessary to represent the true physical situation (e.g. whether and how much aliasing happens of short-scale structure into the long-wavelength tomographic images). The effects of reparametrization are expected to become less relevant, the more finely discretized the respective tomographic model. However, even in case of large numbers of parameters ($\mathcal{O}(10^6)$), they can not be circumvented completely (Simmons *et al.* 2019), since contemporary geodynamic models still have a much higher grid resolution.

The reparametrization is also necessary if one wants to compute the synthetic data using $\mathbf{G}\mathbf{m}^{\mathrm{syn}}$; that is, if the data sensitivity is represented in the tomographic model parametrization. To avoid both the reparametrization as well as the computational costs related to 3-D full waveform simulations, we have chosen in this work to experiment with the direct calculation of ray-theoretical traveltime residuals in the synthetic model using earthquake-receiver locations and seismic phases of the SOLA-Z16 seismic data set. For the ith synthetic, ray-theoretical measurement, we also create some artificial noise component by drawing a random value from a normal distribution $\mathcal{N}(0, \sigma^2_{d_i})$, with standard deviation σ_{d_i} taken to be the uncertainty of the ith datum from the real seismic data set. The generation of the entire noise vector $\mathbf{n}$ and the subsequent computation of the particular corresponding GIP realization is repeated many times for a sufficient number of draws in order to obtain meaningful statistics and model uncertainties (we will further elaborate on this in Sections 3.2 and 4). The use of ray theory is justified here, as we want to generally show the practical feasibility to compute the GIP. Also, the investigation of propagated noise is independent of the way the model traveltime signal is generated. The restriction to ray-theoretical traveltimes thus has no impact on the conclusions of our study, as we are also not aiming at a comparison between GIP models and the tomographic model SOLA-Z16 here.

Altogether, this new approach is a substantial improvement over conventional tomographic filtering with $\mathcal{R}$ (see examples in Sec. 3.1), because we have now the possibility to work with data that have 'seen' the synthetic model and as we can additionally explore various GIP models with a large number of different noise realizations allowing us to consider model uncertainties (see examples in Section 3.2).

3 EXAMPLES OF CONVENTIONAL AND GIP FILTERING

3.1 Conventional filtering

For demonstrating the effects of the SOLA-Z16 tomographic filter and the mapping of synthetic data into model space via $\mathbf{G}^{\dagger}$, we use the geodynamic model *N16-EB16* of Nerlich *et al.* (2016) (for details on the model, see Appendix A). In fact, the exact model setup is not crucial for the current work. Important to note is only that owing to the assimilation of plate motions as surface boundary conditions, the locations of structures in this global mantle circulation model (MCM), in particular cold downwelling slabs, are roughly compatible with those found on Earth (i.e. as seen in tomographic images). This is an important prerequisite for tomographic filtering, as otherwise there would be a mismatch between the model structures and how they would be seen by the uneven seismic data coverage. To perform the necessary reparametrization, we follow the interpolation method of Zaroli (2010) that allows projecting the high-resolution geodynamic model onto the much coarser tomographic grid of SOLA-Z16.

In Fig. 2 the results of the conventional filtering approach using $\mathcal{R}$ of SOLA-Z16 on the model N16–EB16 are shown, including the reparametrization and filtering steps. The two most prominent features of the original model in the mid-mantle are the fast velocity structures around the Pacific belt (especially North- and South America and Southeast Asia) and a half-ring shaped low-velocity structure in the Middle- and South Pacific (Fig. 2a). The general effects of reparametrizing the model on the irregular grid of SOLA-Z16 are a broadening of anomalies and a reduction of their magnitude, which are more severe in regions of lower grid node density, as expected (Fig. 2b). After filtering with $\mathcal{R}$, most features are further spread out and an additional reduction of magnitude is apparent, which overall leads to coherent large-scale anomalies in the transition zone and upper mid-mantle in the filtered model (Fig. 2c). For example, a distinct low velocity structure appears in the North Pacific, at a depth between 400 and 1310 km, with a maximum amplitude and extent between 810 and 960 km. This is probably related to vertical smearing of structure from the upper mantle, due to the averaging kernels of SOLA-Z16 that reach from the mid-mantle almost up to the surface in this area. Plotting those averaging kernels at a certain location would make it possible to spatially isolate this effect, which however is not the scope of the current study. Having the conventionally filtered models at hand, we have a clear expectation on how the effect of limited resolution inherent to the SOLA-Z16 filter alters the original model. On the other hand, this classical filtering procedure entirely ignores the range of possible models that would be conceivable if tomographic model uncertainties were considered, which is in fact realized by computing GIP models.

3.2 New filtering based on the GIP

3.2.1 Examples of GIP realizations

In Fig. 3 one of the many possible GIP models is shown, which can be computed from the synthetic traveltime data in the MCM with the method introduced in Section 2.3. In addition to the GIP model obtained with added random noise (Fig. 3a), we also present the GIP model without noise (Fig. 3b) and the propagated noise alone (Fig. 3c); that is, the contribution of this specific noise realization to the model resulting from $\mathbf{G}^{\dagger}\mathbf{n}^{\mathrm{syn}}$. On large scales, the GIP models

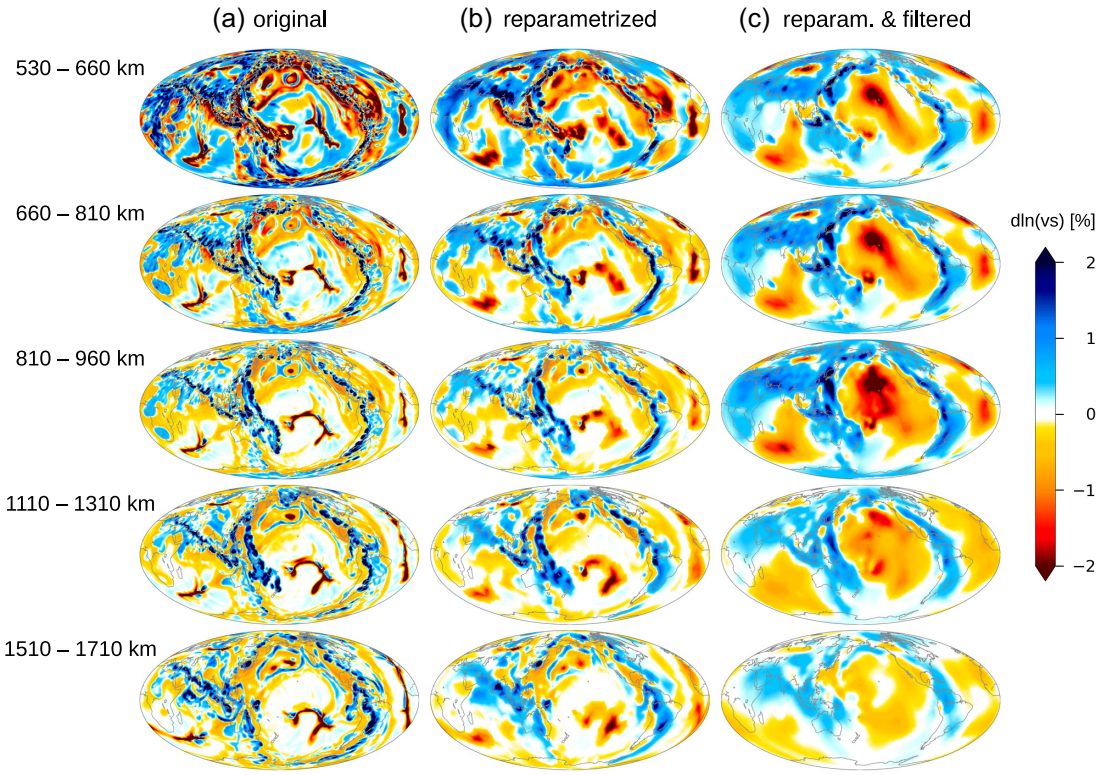

Figure 2. Global maps of shear velocity variations of model N16-EB16 for five depth layers: (a) the original model averaged over the respective depth range; (b) the reparametrized version of the MCM and (c) the tomographically filtered version. Variations are given relative to the corresponding average 1-D model of the MCM. Reparametrization and filtering together lead to considerable smearing of anomalies and a reduction of the heterogeneity amplitudes.

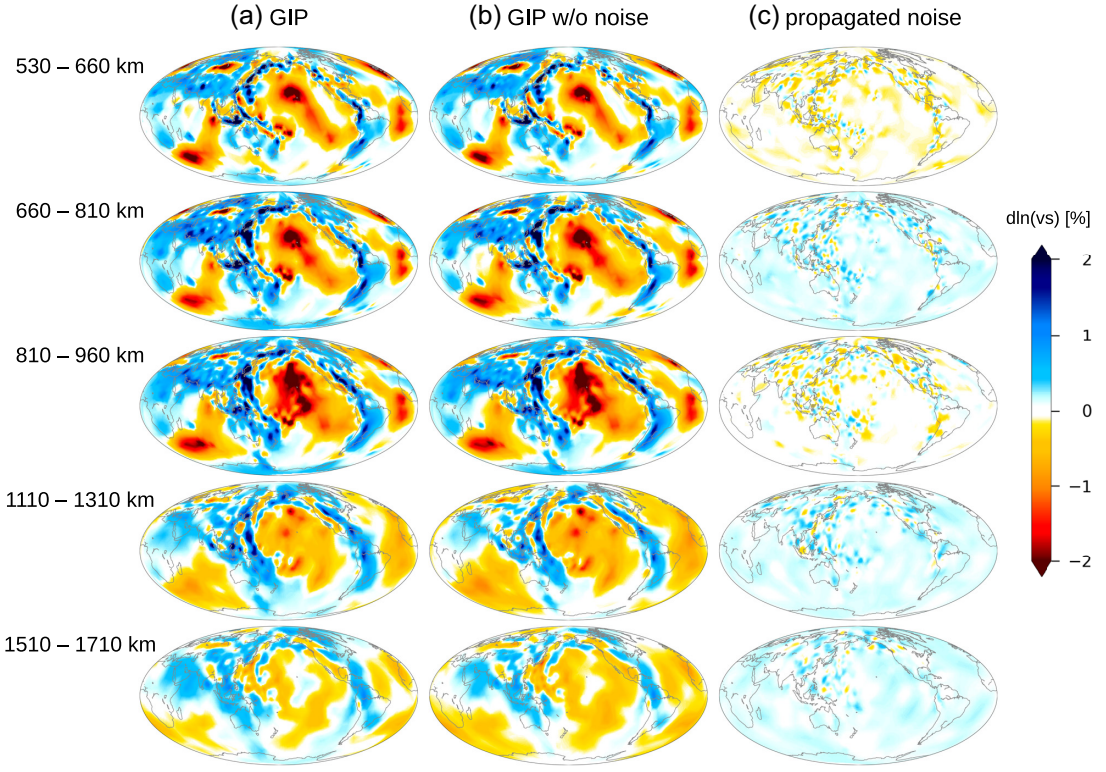

Figure 3. Global maps of (a) the GIP model for one specific realization of noise; (b) the same GIP model without (w/o) noise. (c) Global maps showing where the noise ends up in the model solution in case of the specific noise realization of (a). Note that column (a) is the sum of columns (b) and (c).

with and without noise do not seem to differ severely for this noise realization, but a closer look reveals some differences on smaller scales that may play a role for geodynamic interpretations, for example the exact shape of the low velocity structures in the Pacific region. It is also clear from Fig. 3(c) that the noise in the data contributes significantly to the final model estimate. The heterogeneity structure induced by the propagated noise is apparently linked to the irregular grid of SOLA-Z16, because pronounced small-scale patterns are mostly present in regions of higher grid density, i.e. better resolution. Remember that in SOLA B–G tomography, better resolution commonly means larger model uncertainties and therefore a larger contribution of noise propagating into the model solution. In Fig. 3(c) one can also observe a distinct difference between the layers, where in regions of lower grid density the propagated noise leads to either a positive or negative shift, which changes the overall strength of anomalies between the GIP models with and without noise. Note, however, that this is only one possible GIP model from a large suite of models that cover the range of model uncertainties given by the SOLA-Z16 inversion. Furthermore, we note that the model resulting from the GIP approach also resembles the tomographically filtered model that is simply based on $\mathcal{R}$, but here, they are not strictly identical (see Section 4).

3.2.2 *Effects from projected noise*

In a next step, we want to consider a large number of GIP models to investigate the effects of the full range of possible noise realizations and how this varying noise propagates into model space. This is an important step in that any tomographic image itself is just the result of an inversion based on one specific noise realization incorporated in the real-world measurements (estimated to each lie within one standard deviation of the respective true datum). This also implies that for any comparison of a geodynamic model and a tomographic image, the range of uncertainties should be considered for the former, as only for the geodynamic model, the true mean model is known. To explore this range, we redo the sampling of $\mathbf{n}^{\mathrm{syn}}$ from the set of normal distributions $\mathcal{N}(0, \sigma_{d_i}^2)$ one thousand times to construct a set of GIP models, each corresponding to one realization of the noise. Fig. 4 shows maps of four different GIP models at a depth of 1510–1710 km: the GIP model without noise and three selected GIP models that were computed with different noise realizations. We show contour lines at a level of 0.25 per cent $dln(vs)$ for easier identification of local differences in the models with respect to the GIP model without noise. This contour level corresponds to a typical threshold in global tomography above which heterogeneities may be interpreted as robust features. In each map, the 0.25 per cent contour of the noise-free GIP model is shown with a black solid line for comparison, while the respective contours of the GIP models with noise are depicted with a blue dashed line. GIP model #1 (upper right panel, same model as in Fig. 3b) displays mostly an increase of the lateral extent of positive velocity anomalies (i.e. those above the threshold). However, the slab in the Northern Pacific apparently is separated into two parts here. GIP model #60 (lower left panel) shows an even stronger increase in the extent of fast structures, with the most striking feature of an elongated positive anomaly in the Mid-Pacific south of Hawaii. In contrast, GIP model #200 (lower right panel) features a strong decrease of fast seismic anomalies and much stronger negative velocity anomalies, which leads to less coherent and much more fragmented slabs. In particular, the comparison between the noise-free GIP model and GIP #60 reveals the importance of a correct treatment of uncertainties in the interpretation of tomographic images: In the latter, one would be tempted to interpret the 'slab' in the middle of the Pacific at mid-mantle depths as a robust feature with all its geologic consequences, while from the GIP model without noise one would argue for 'normal mantle', which corresponds also to the underlying structure in the original MCM (Fig. 2a) at that location. To some extent, the effects of noise might be mitigated by removing the mean value from each layer of the models as is common practice in many tomographic studies. This, however, bears the danger of skewing the statistics of the model uncertainties, which renders any evaluation or further use more difficult. Here, we do not modify the models in such a way, but rather keep the full noise effects for further analysis.

3.2.3 *Statistical properties of projected noise*

One important quantity that typically is computed for tomographic models, and used for interpretations as well as for comparisons to geodynamic models, is the average strength of heterogeneities in each depth layer as given by the root-mean-square (RMS) of all model parameters at one depth. In Fig. 5 we show distributions of RMS profiles calculated for the set of 1000 GIP models to quantify the variability in the average 'imaged' strength of seismic heterogeneity in our case. In our framework, the RMS can be computed separately for each layer l with L grid nodes as

$$\mathrm{RMS}(\hat{\mathbf{m}}^{\mathrm{GIP}})_l = \sqrt{\frac{\sum_{k=1}^{L} V_k (\hat{m}_k^{\mathrm{GIP}})^2}{\sum_{k=1}^{L} V_k}}\,, \tag{18}$$

where k is the local grid node index and V_k the volumetric weights corresponding to the SOLA-Z16 tomographic grid (see also eq. 12). The RMS distributions vary considerably with depth with generally larger variances at greater depths. Important to note is that the extreme values in the various layers are unrelated; that is, not related to a single 'extreme' model. Put differently, the model with maximum RMS (out of the 1000 models) in one layer does not necessarily give rise to the maximum RMS in other layers. To get an impression of the entire RMS distributions, we chose to use violin plots to infer a continuous probability distribution from our limited set of 1000 GIP models. All distributions are positively skewed, meaning that RMS outlier models show mainly stronger heterogeneity. Also, the profile of the GIP model without noise is close to the minimum at each layer, which suggests that the addition of noise seems to commonly increase the imaged heterogeneity on average. In the transition zone, RMS variations are moderate and the values do not differ by more than 0.1 per cent $dln(vs)$. At depths of 810–960 km, the range of RMS amplitudes is at a minimum, which could be related to the observation that in our data set many ray paths of *SS* waves are bottoming in this region or because this is the first layer where any rays are actually turning. For the remaining mid-mantle layers, the variation of RMS is larger, so that values may differ by up to 0.2 per cent $dln(vs)$. Since the distributions are inferred from merely a 1000 GIP models they can of course not cover the population of possible models. Consequently, we tried to give reasonable lower and upper bounds for the expected RMS amplitudes using two GIP models, one in which we increased the magnitude of traveltime residuals by their corresponding standard deviations from the SOLA-Z16 data and one where we decreased the magnitude this way (ignoring in this case the importance of covariance). Note that those bounds can not be seen as extreme values or confidence intervals for the RMS, but rather represent an approximate range where we expect most GIP models to fall within.

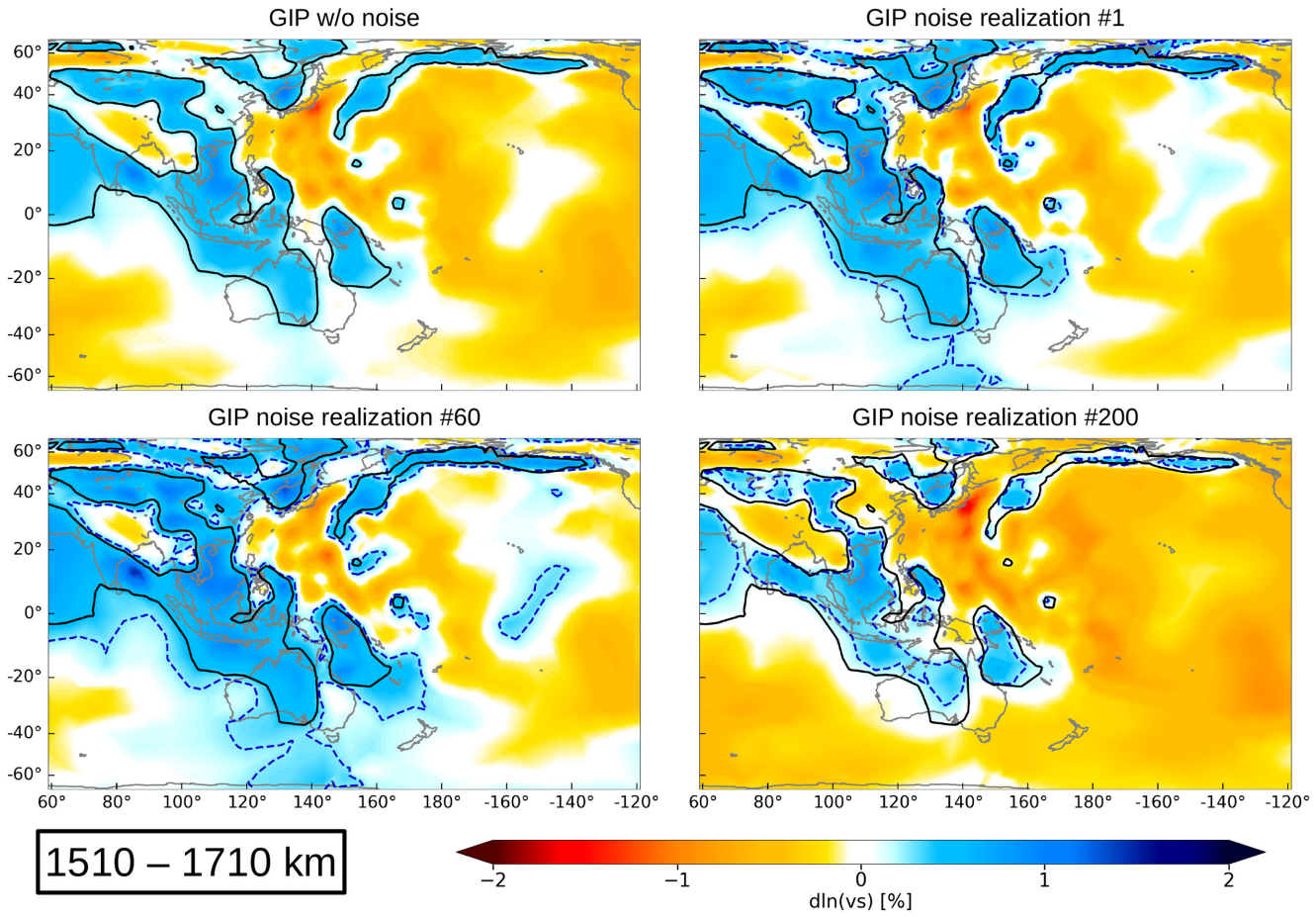

Figure 4. Effect of varying noise realizations on GIP models. Contour lines are shown at a level of 0.25 per cent d$ln(vs)$ to give an impression of what could be considered as reliably imaged fast structures. In each plot, black contour lines show the structure of the GIP model without noise and blue dashed lines show the same contour level in the corresponding GIP model including a specific noise realization. Comparison of all four panels illustrates that certain tomographically imaged features, like what appears to be a slab structure in middle of the Pacific in case of noise realization #60, might not be as robust as initially considered. Note that we do not remove the mean value from each layer of the GIP models, which is common practice in many tomographic studies, as this bears the danger of skewing the statistics of the model uncertainties in the further course of this work.

In order to quantify the amount of propagated noise, we chose to use 1000 GIP models as a compromise between computational effort and a relevant sample size and computed RMS values. This limited number of models of course affects the capability to generalize our findings on the distribution of RMS values, as one cannot directly calculate or estimate the true distribution from a finite set of data. Therefore, we have to treat the RMS results with some caution, although we think that the general trend can be delineated. Also, considering eq. (18), our RMS distributions can be qualified as the square-root of the linear combination of dependent scaled non-central chi-squared distributions. Such distributions can not generally be computed analytically and numerical solutions only exist for much 'simpler' cases, for example the linear combination of independent chi-squared distributions (Bausch 2013). In our case, computing GIP models is thus a necessary step to quantify the expected mantle heterogeneity with RMS from uncertainty information, and it will be necessary in future to develop a scheme for deciding between acceptable models and statistical outliers.

We now come back to looking at individual model parameters, and note that independent from the noise-free GIP model, we can analyse the corresponding 1000 GIP realizations of $\mathbf{G}^{\dagger}\mathbf{n}^{\mathrm{syn}}$ to see where the propagated noise ends up in model space (see Fig. 6, upper rows). We computed from the total set of GIP models the mean value for each model parameter for the depth ranges of 530–660 km and 1110–1310 km and also show maps in which the standard deviation at each parameter is subtracted or added, respectively. The observation that the mean model is 'white' indicates that the set of 1000 GIP models provide an adequate sampling of each model parameter. Thus it comes as no surprise that the maps considering the standard deviations show approximately the model uncertainties of SOLA-Z16, which are evidently linked to the data-driven structure of the irregular tomographic grid.

3.2.4 Exploring the effects of systematic errors

The general assumption in most tomographic applications is that the data uncertainty follows a normal distribution. This, however, could be a rather strong assumption given the many sources of uncertainty in seismic data, especially if systematic errors from inadequate modelling are present. Therefore, one may wonder how filtered models would look like if the noise in the real data was not normally distributed around zero. For example our imperfect knowledge of the crust or frequency-dependent crustal effects (Dubois *et al.* 2019) may lead to wrong crustal corrections that can be interpreted as a systematic bias in the noise term. How would $\mathbf{G}^{\dagger}$ project this biased

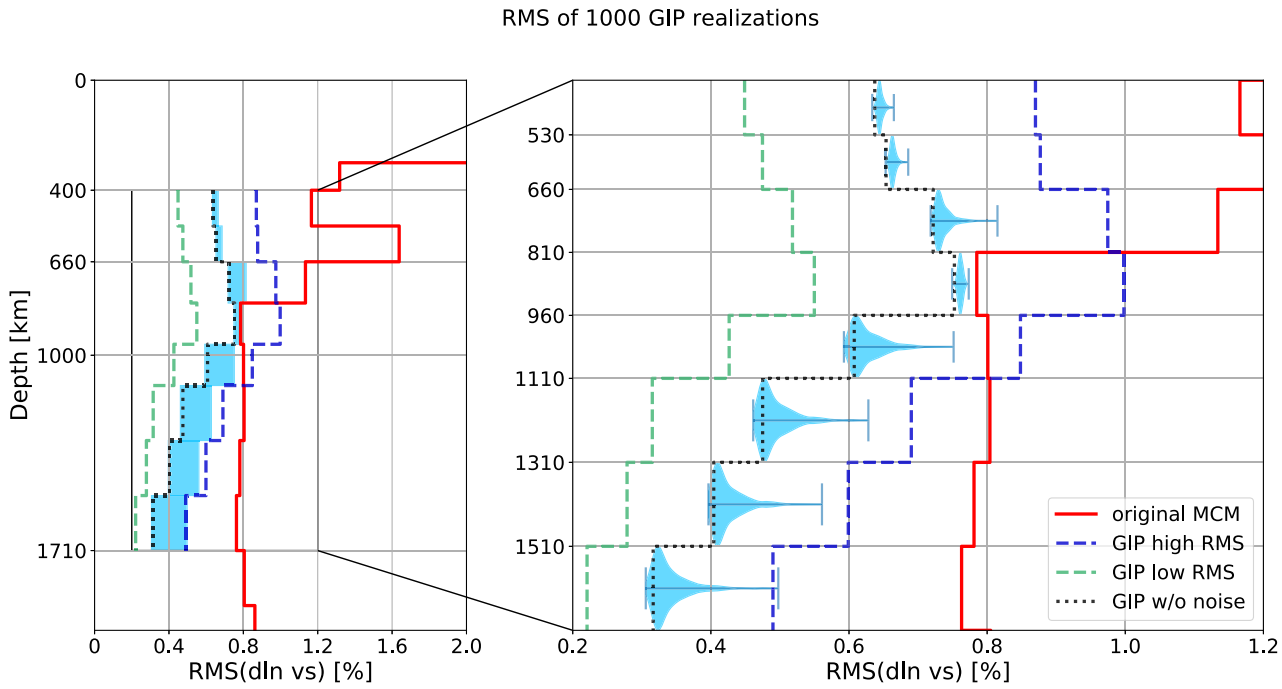

Figure 5. Distribution of RMS values estimated from a set of 1000 GIP models that are computed using independent noise realizations (right-hand panel; light blue violin plots). The RMS profile of the GIP model without noise (black dotted line) does not always coincide with the peak of the inferred RMS distributions from the set of 1000 GIP models. Maximum RMS values (blue dashed line) result from a GIP model in which the seismic noise was artificially chosen such as to increase, for all at the same time, the magnitude of the synthetic traveltime residuals by their respective standard deviation σ_{d_i}, whereas the minimum RMS (green dashed line) results from decreasing all residual magnitudes by σ_{d_i}. Note that in the case of those two extreme RMS profiles, the covariance of the data and model parameters are neglected.

noise into model space and how would model uncertainties change? Taking the crustal effects as one example, we try to give a quantitative answer to this question by considering again a large set of noise realizations in which such a systematic component of noise from crustal corrections is added to the random noise. In the case of systematic biases, this approach is kind of a Monte Carlo error propagation strategy to quantify model uncertainties (see e.g. Aster *et al.* 2005). Since we do not know the uncertainties of crustal travel times, we may reasonably estimate the potential bias they could cause by calculating the difference between traveltimes in models CRUST1.0 $\delta t_i^{\text{crust1.0}}$ (Laske *et al.* 2013) and CRUST2.0 $\delta t_i^{\text{crust2.0}}$ (Bassin *et al.* 2000) for each ray path of the SOLA-Z16 data set. We are aware of the fact that other choices for the two crustal models could have been made, and as both CRUST1.0 and CRUST2.0 are coming from the same research group, we consider our choice as a conservative estimate of the crustal noise bias. Considering that the crustal models are themselves uncertain, we can treat the traveltimes in each crustal structure as random variables which we assume to follow a normal distribution $\mathcal{N}(\delta t_i^{\text{crust1.0/2.0}}, \sigma^2_{\text{crust}})$, where $\delta t_i^{\text{crust1.0/2.0}}$ are the traveltimes in the crust that were actually computed for each source-receiver configuration using ray theory, and σ_{crust} is the standard deviation of the traveltime differences $\Delta t_i^{\text{crust}} = \delta t_i^{\text{crust2.0}} - \delta t_i^{\text{crust1.0}}$ of all ray paths. We compute again one thousand realizations of the systematic noise component by drawing random realizations $dt_i^{\text{crust1.0/2.0}}$ from both corresponding normal distributions and computing their difference $dt_i^{\text{crust2.0}} - dt_i^{\text{crust1.0}}$. Each realization of the biased noise $\mathbf{n}^{\text{bias}}$ is thus given by

$$\mathbf{n}^{\text{bias}} = \mathbf{n}^{\text{syn}} + (\mathbf{dt}^{\text{crust2.0}} - \mathbf{dt}^{\text{crust1.0}}), \tag{19}$$

which we finally use to get one thousand realizations of the propagated biased noise $\mathbf{G}^{\dagger}\mathbf{n}^{\text{bias}}$.

Fig. 7 compares histograms of the set of realizations of biased and unbiased noise for three different ray paths. In general, the bias that we introduce leads to a shift of the mean away from zero and a broadening of the distribution quantified by higher (sample) standard deviations depending on the exact source-receiver configuration and the structural differences between the two crustal models. Owing to its non-zero mean, one can see in Fig. 6 that the resulting mean model of the propagated biased noise is no longer white (i.e. the mean contribution to the seismic heterogeneity is not zero any more), as in case of the propagated random noise. For the layer between 530 and 660 km one can clearly see an imprint of the crust in the mean model, which is dominated by a positive signal in the oceans and a mostly negative one on the continents. Interestingly, the propagated biased noise shows a sharp contrast approximately across the Date Line in the Pacific. We made different tests with the generalized inverse operator to ensure that this is not an artefact, and we found that it can be explained by the combination of effects from the difference in crustal models, the shape of the tomographic grid, the way $\mathbf{G}^{\dagger}$ acts on the input data and the source–receiver configurations of the tomographic data set (see Fig. 1 and Fig. S2 in the supplementary material). Also in the layer between 1110 and 1310 km there is a notable model response to the biased noise that is however less strong than in the upper layer. In addition to the mean model we subtracted or added, respectively, the standard deviation at each model parameter from the set of 1000 models to indicate how strong values may locally vary. This suggests that the presence of systematic biases—which the GIP method is able to handle as an additional noise term—can alter the way we see the true Earth

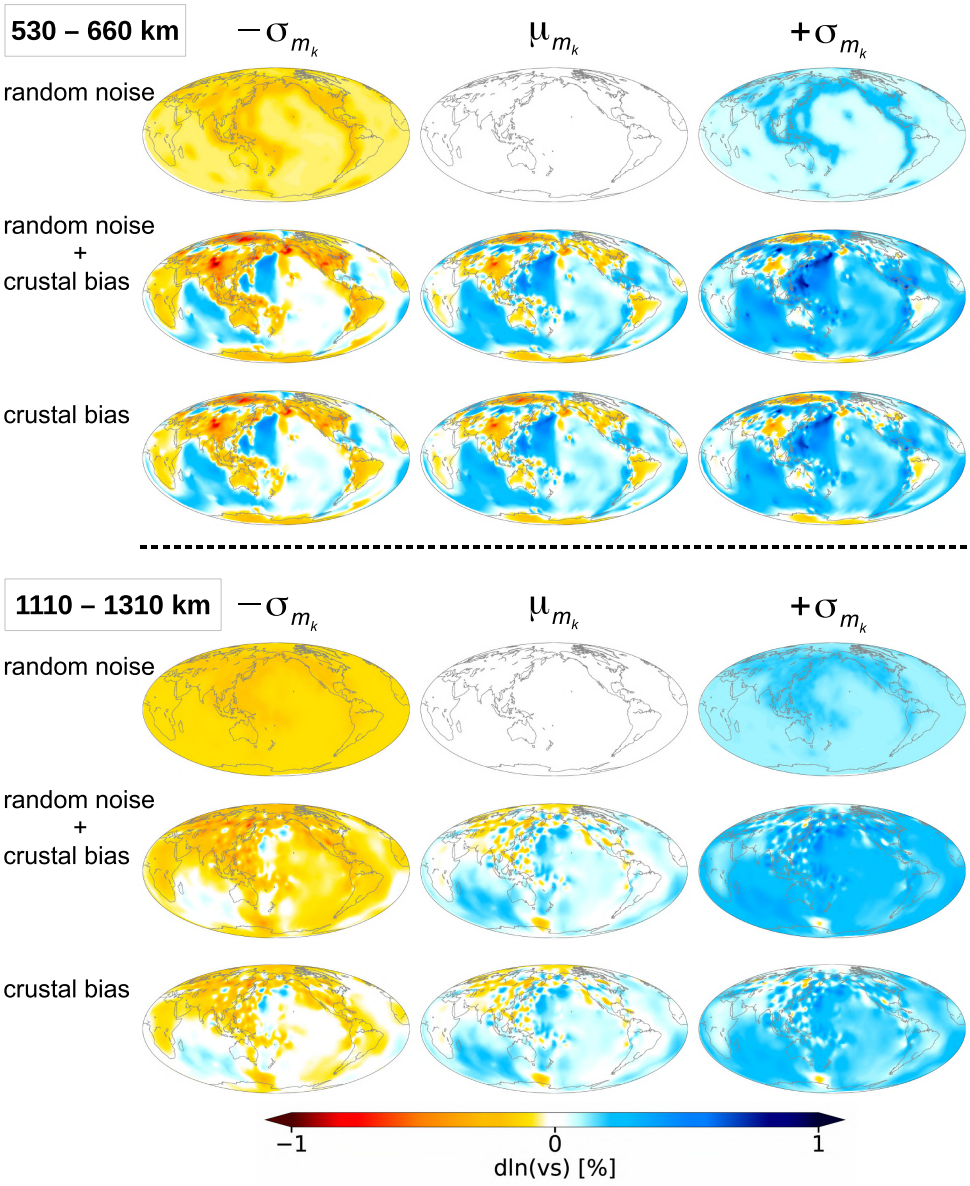

Figure 6. Statistics of the projected noise from the set of 1000 GIP realizations for two depth ranges. In each row, the maps show the mean (middle column) and ± standard deviation (right- and left-hand column, respectively) at each model parameter. For each depth, the top row shows the statistics for the Gaussian zero-mean random noise based on the noise assumptions from the SOLA-Z16 tomographic model, while the middle row shows the effects of adding to it a biased-noise component related to uncertain crustal structure. The bottom rows illustrate the model uncertainty in case of the biased-noise component alone.

with linear seismic tomography, which may lead in the worst case to incorrect model interpretations.

4 DISCUSSION AND PERSPECTIVES

In Section 3.2, we demonstrated that computing a suite of GIP models is a viable approach to investigating the effects of both limited resolution as well as uncertainties. Key to this method is the explicit knowledge of the generalized inverse $\mathbf{G}^{\dagger}$ that maps synthetic data and noise to the model space. Based on the GIP approach, we provided a quantification of model uncertainties resulting from realistic realizations of noise in the seismic data. As expected, the various noise realizations significantly alter the 'filtered' models. This is true not only for the morphology of structures and the average seismic heterogeneity as quantified, for example, with RMS profiles, but also for the apparent strength of single anomalies. This can, as our results show, lead in the worst case to misinterpretation of mantle dynamics owing to 'structures' that actually are not present in the noise-free model and, even more important, in the underlying 'true' Earth. This implies that for a comprehensive link between seismic information and geodynamic considerations, uncertainties in the seismic data play a vital role and should always be considered.

A typical scenario in Earth in which this would come into play is the seismic structure of the mantle below hot spots and the question of whether it is associated with deep mantle-upwellings (i.e. plumes) rising from a thermal boundary layer at the CMB (e.g. Montelli *et al.* 2004; French & Romanowicz 2015; Chang *et al.* 2016). It is known that the detectability of such features, especially in the deeper

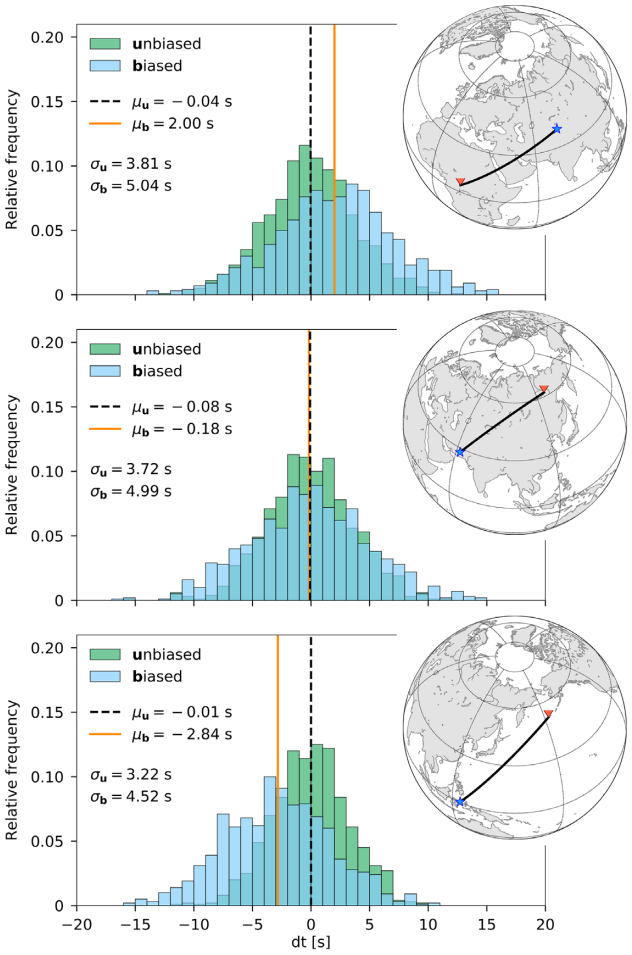

Figure 7. Histograms for three examples of unbiased (u) and biased (b) noise realizations of specific ray paths. Maps in the upper right corner of each panel depict the corresponding source-receiver configuration (blue star and red triangle, respectively). Additionally, the sample mean and standard deviation of the unbiased and biased noise data are given.

mantle, depends on the data coverage, the technique used to solve the forward and inverse problems and other factors (Maguire *et al.* 2018). To answer the question of the existence of a given structure, it is necessary to quantify resolution as well as noise that propagates into the tomographic solution and to then assess the resulting images in the light of this additional (and non-negligible) information. However, a straight-forward appraisal of tomographic images is currently impracticable with full-waveform or probabilistic inversions (e.g. Fichtner & Trampert 2011; Rawlinson *et al.* 2014). An alternative that will have the potential to robustly constrain the very nature of those features could be to perform an analysis based on the GIP approach using geodynamic models constructed from consistent physical and mineralogical considerations while having at hand and dealing with all possible uncertainties (not only in the seismic data, but also in the mineralogical and geodynamic parameters). As we have illustrated, the quantification of the effects of seismic data uncertainty in the model space can be solved elegantly with the SOLA B–G generalized inverse, and the accurate assignment of the data (co-)variance then in fact constitutes the main challenge.

Having available good estimates of the seismic data uncertainties and, in particular, a way to map them into model space is going to be a crucial component not only for the assessment of geodynamic forward models, but even more so for inverse models of mantle convection. Retrodictions of the past evolution of the mantle via adjoint geodynamic simulations depend on estimates of the state of the mantle at present-day in terms of buoyancy, and tomographic models serve as the basis for this estimation. As with any inversion, the way the misfit functional is stated is of fundamental importance, influencing what actually is propagated back in time as the adjoint field. In the case of geodynamic adjoints, one typically computes local differences between an initial 'first-guess' forward-modelled field at present day and the tomographic estimate. In this process, it is on the one hand vital to understand the effects of resolution, as this will have direct impact on the misfit calculation. Generally, one expects structures in the forward-modelled geodynamic field to be represented on shorter scales than the structures resolved with currently available seismic data and tomographic methods. Furthermore, to learn about the behaviour of Earth's mantle from its evolution over time in comparison to the geologic record, it will be crucial to investigate not only a single model, but an ensemble of models based on a set of different tomographic estimates. Such a suite of tomographically derived mantle states can, with the method introduced in this study, be generated conveniently using the SOLA B–G generalized inverse. Given the uncertainties of the seismic data, one can obtain a range of different tomographic realizations—by random sampling of the data uncertainty distribution—that will cluster around the mean tomographic model. It is clear that a sufficiently large number of drawings is required to provide a good coverage of the posterior model covariance (e.g. in our case, 1000 random draws appeared to be sufficient). As the geodynamic adjoint simulations pose a massive computational challenge, it may be unfeasible to run inversions back in time for such large ensembles, and future research needs to be directed towards finding ways of how to best represent tomographic model uncertainty in such applications with a limited number of noise realizations.

Given the above considerations, it is important to discuss the role of seismic noise in more detail. In the statistical framework applied in our approach, we may regard the vectors $\mathbf{d}$ (including noise) and $\hat{\mathbf{m}}$ as random variables, in which each entry follows a normal distribution with a specific mean and variance. In this case, the mean of $\hat{\mathbf{m}}$ is given by the GIP model without noise, while models deviating from the mean model include a particular amount of propagated noise that is statistically described at each model parameter with a corresponding uncertainty. For the interpretation of these uncertainties in context of the model space, it is however not sufficient to merely look at the variance of individual parameters (which is an explicit output of the SOLA B–G method). Rather, it is necessary to deal with the covariance of model parameters, which is implicitly incorporated in our method by applying $\mathbf{G}^{\dagger}$ to the synthetic data set including a large number of particular noise realizations.

Having an estimate of the model covariance matrix $\mathbf{C}_m$—representing the uncertainties and inter-correlations of 'individual' parameters m_k—is important for several applications such as not only the problem of geodynamic retrodiction, but also for computing uncertainties of seismic travel times predicted by a given tomographic model (Simmons *et al.* 2019). Although we do not explicitly state the SOLA B–G model covariance matrix, $\mathbf{C}_{\hat{m}}$, in this study, it would be straightforward to calculate it as

$$\mathbf{C}_{\hat{m}} = \mathbf{G}^{\dagger}\mathbf{C}_d(\mathbf{G}^{\dagger})^T \,, \tag{20}$$

with the (diagonal) data covariance matrix $\mathbf{C}_d$. It is important to bear in mind that, within the SOLA B–G inversion scheme, the model estimates $\hat{m}_k$ represent some 'weighted averages' of the true-model parameters, spatially localized around each point $\mathbf{r}_k$ (noting that a

specific averaging volume may still encompass several grid points). Hence, the SOLA B–G model covariance matrix $\mathbf{C}_{\hat{m}}$ represents the propagation of data noise into these averages (i.e. given by the diagonal elements $\sigma^2_{\hat{m}_k}$), and how these averages are intercorrelated. However, in the general case, it cannot inform us on how much the value of $\hat{m}_k$ may differ from the true-model parameter m_k—at least when the spatial variations of m are non smooth and/or the spatial extent of the kth resolving kernel is far from a Dirac delta function (Zaroli 2019). Still, in case of spatially varying parametrizations adapted to the data coverage and corresponding choices of the target resolving kernels, the unbiased SOLA B–G averages $\hat{m}_k$ may be localized enough to sufficiently represent the true-model parameters m_k, so that $\mathbf{C}_{\hat{m}}$ is also a good approximation of the actual model covariance $\mathbf{C}_m$ related to the individual parameters. Future research will be necessary in this direction to better understand the effects of parametrization as well as the choice of target kernels and trade-off parameters.

A few additional remarks: For large tomographic problems in general, it may be unfeasible to obtain the full model covariance matrix, because its direct calculation becomes a computationally challenging task requiring efficient numerical algorithms that often rely on matrix factorization techniques (e.g. Soldati *et al.* 2006; Ballard *et al.* 2016; Bogiatzis *et al.* 2016). In another approach to computing model covariances for the tomographic model LLNL-G3D-JPS with $\mathcal{O}(10^6)$ parameters, Simmons *et al.* (2019) approximated the resolution matrix $\mathcal{R}$ using a multiple-impulse response strategy for reducing the computational burden and used it together with an *a priori* covariance matrix to get an *a posteriori* covariance $\mathbf{C}_m^{\text{post}} = (\mathbf{I} - \mathcal{R})\mathbf{C}_m^{\text{prior}}$ (see e.g. Tarantola 1987). However, they report that they had to correct for unreasonable covariance estimates and the need to condition the matrices such that they become easier to handle for some practical applications, for example the calculation of path-specific traveltime uncertainties. Note that one cannot incorporate some *a priori* model covariance in the SOLA B–G method, which may seem as a drawback of the method. In our view this can be advantageous, as it avoids the need of having to incorporate some *ad hoc*, often unphysical, *a priori* model constraints. In studies using Bayesian inference, the choice of the prior probability distribution is a critical issue and the probabilistic inversions are typically based on the assumption of zero-mean Gaussian statistics. As we have shown in this study, the latter assumption is not necessary in the GIP approach with SOLA B–G. Furthermore, probabilistic inversions are hampered by the curse of dimensionality (e.g. Sambridge *et al.* 2013; Fichtner *et al.* 2018), and thus are currently unpractical for large tomographic inversions that may, for example, comprise the whole mantle using a relevant data coverage. For such problems, the GIP approach can still be used to represent the information content of $\mathbf{C}_m$ without the need to fully state it, as the calculation of $\mathbf{G}^\dagger$ is computationally highly efficient and easily parallelizable in SOLA B–G inversions. In other words, it would still be trivial to calculate GIP models (and thus consider model covariance) even for very large tomographic problems. In this respect, it is worth mentioning that it would also be possible to estimate the model covariance matrix of SOLA B–G by computing the so-called sample covariance matrix $\tilde{\mathbf{C}}_{\hat{m}}$ from a set of propagated noise models ($\mathbf{G}^\dagger\mathbf{n}^{\text{syn}}$). Together with the advantage that no reparametrization of models is necessary, the GIP approach may therefore prove very useful in future applications.

Apart from the examples of using the GIP approach shown in this study, there is a broad range of further applications. A quantitative comparison between MCM models and a SOLA B–G tomography that specifically focuses on a full incorporation of resolution and uncertainty will obviously be the subject of future work. Such comparisons should preferably feature models of the whole mantle, and efforts to obtain a global SOLA model are currently under way (see Dubois 2020). A practical tool for the comparisons could further be to plot SOLA B–G's averaging kernels in order to visualize resolving volumes and to explain effects of smearing and lacking data coverage. For the generation of the synthetic data in the geodynamic model, it would also be favourable to compute travel times using finite-frequency sensitivity instead of ray-theory. This would reduce the difference between the tomographically filtered version of the synthetic model and the noise-free GIP model to the effect of reparametrization that is inherent to the classic approach (see supplementary figures). Also, recently (Zaroli 2019) moved the SOLA B–G inversion scheme from a discrete to a continuous model representation named 'parameter-free SOLA tomography'. In this method it is now possible to fully make use of the data sensitivity kernels for the inversion, as they do not need to be projected on an often coarse tomographic grid as is the case in parameter-based inversions. Applying this parameter-free scheme in a global context and using the GIP approach introduced here could dramatically sharpen our view of mantle structure and give us a reliable tomographic basis for answering related geodynamic questions.

5 CONCLUSIONS

In this proof-of-concept study, we have presented the GIP as a novel approach for computing tomographically filtered synthetic models of Earth's mantle. In this approach, it is possible to account not only for the limited resolution, but also for the effects of noise (i.e. errors) in the seismic data allowing for systematic investigations of tomographic model uncertainties. A particular GIP model is generated by applying the generalized inverse operator $\mathbf{G}^\dagger$ to a synthetic seismic data set calculated in a 'true' mantle model to which a random noise contribution can be added. Explicit knowledge of the generalized inverse operator thus is a prerequisite to be able to apply this method. In the specific case considered here, we took advantage of the recently introduced SOLA Backus–Gilbert tomographic inversion, in which $\mathbf{G}^\dagger$ can efficiently be calculated for tomographic problems on a global scale. To illustrate the potential of the GIP approach, we applied $\mathbf{G}^\dagger$ of Zaroli (2016) to a synthetic set of traveltime variations computed in a mantle circulation model. A large number of noise realizations were generated by repeatedly drawing random values from zero-mean normal distributions with standard deviations given by the uncertainty of each individual datum as estimated in the original SOLA-Z16 tomographic model. The projection of noisy synthetic data via the generalized inverse then demonstrates where and in which way, data uncertainties might end up in model space. We found significant differences between the various GIP realizations, which highlights the importance of interpreting and assessing tomographic images in a prudent and cautious manner.

For the entire ensemble of GIP realizations, the mean of the model parameters is equivalent to the GIP model for the noise-free data in case of Gaussian random noise, as expected for a large number of drawings. In other words, the mean contribution of random noise is zero. Besides looking at random noise, we demonstrated that it is also possible to project noise components to the model space that exhibit systematic deviations from a typically assumed Gaussian distribution. To provide an example of such a biased noise

contribution, we looked at systematic errors related to the crustal correction and imperfectly known crustal structure that potentially affect tomographic inversions. The GIP models were significantly altered by the biased noise propagating into the model solution compared to the initial case with random noise. In particular, the mean of the biased-noise contribution in model space no longer is zero. The great potential of the GIP approach therefore lies in the fact that one is able to specifically quantify the contribution of systematic data errors in model space. It will thus be increasingly important to have good estimates for such uncertainties available in future.

In addition to investigating the effects of the biased noise on the mean model, we looked at the (co-)variance of model parameters. In case of random noise, the SOLA B–G tomographic inversion scheme can provide the individual model uncertainties directly, which is not possible any more in case of systematic errors. Future research needs to be directed towards understanding how to include the model covariance information—that can be obtained with the GIP approach—in geodynamic simulations. In other words, the uncertainty in the initial seismic data needs to be systematically explored in future geodynamic modelling efforts. For example, for the retrodictions using geodynamic adjoints, it will be important to provide estimates of the present-day thermodynamic state of the mantle in a statistically meaningful manner.

ACKNOWLEDGEMENTS

We want to thank the editor Ian Bastow as well as Andreas Fichtner and an anonymous reviewer for constructive comments that helped to improve the manuscript. We are also grateful to Paula Koelemeijer and Isabel Papanagnou for fruitful discussions on this study and helpful comments on the initial version of this article. This work was supported by the Programme National de Planétologie (PNP) of CNRS/INSU, co-funded by CNES. RF received support from the ERASMUS+ Programme.

REFERENCES

Aster, R., Thurber, C. & Borchers, B., 2005. *Parameter Estimation and Inverse Problems, International Geophysics Series,* Elsevier Science.

Backus, G.E. & Gilbert, J.F., 1967. Numerical applications of a formalism for geophysical inverse problems, *Geophys. J. Int.,* **13**(1–3), 247–276.

Backus, G.E. & Gilbert, J.F., 1968. The resolving power of gross Earth data, *Geophys. J. Int.,* **16**(2), 169–205.

Backus, G.E. & Gilbert, J.F., 1970. Uniqueness in the inversion of inaccurate gross Earth data, *Phil. Trans. R. Soc. Lond., A,* **266,** 123–192.

Ballard, S., Hipp, J.R., Begnaud, M.L., Young, C.J., Encarnacao, A.V., Chael, E.P. & Phillips, W.S., 2016. SALSA3D: a tomographic model of compressional wave slowness in the Earth's mantle for improved travel-time prediction and travel-time prediction uncertainty, *Bull. seism. Soc. Am.,* **106**(6), 2900–2916.

Bassin, C., Laske, G. & Masters, G., 2000. The current limits of resolution for surface wave tomography in North America, *EOS, Trans. Am. Geophys. Un.,* **81**(48), F897, Fall Meet. Suppl., Abstract S12A-03.

Bausch, J., 2013. On the efficient calculation of a linear combination of chi-square random variables with an application in counting string Vacua, *J. Phys. A,* **46** (50), doi:10.1088/1751-8113/46/50/505202.

Becker, T.W. & Boschi, L., 2002. A comparison of tomographic and geodynamic mantle models, *Geochem. Geophys. Geosyst.,* **3**(1), 1003.

Bogiatzis, P., Miaki, I. & Davis, T.A., 2016. Towards using direct methods in seismic tomography: computation of the full resolution matrix using high-performance computing and sparse QR factorization, *Geophys. J. Int.,* **205**(2), 830–836.

Bolton, H. & Masters, G., 2001. Travel times of *P* and *S* from the global digital seismic networks: implications for the relative variation of *P* and *S* velocity in the mantle, *J. geophys. Res.,* **106**(B7), 13 527–13 540.

Boschi, L., 2003. Measures of resolution in global body wave tomography, *Geophys. Res. Lett.,* **30**(19), doi:10.1029/2003GL018222.

Bull, A., McNamara, A. & Ritsema, J., 2009. Synthetic tomography of plume clusters and thermochemical piles, *Earth Planet. Sci. Lett.,* **278**(3–4), 152–162.

Bunge, H.-P. & Baumgardner, J., 1995. Mantle convection modeling on parallel virtual machines, *Comp. Phys.,* **9,** 207–215.

Bunge, H.-P., Hagelberg, C.R. & Travis, B.J., 2003. Mantle circulation models with variational data-assimilation: inferring past mantle flow and structure from plate motion histories and seismic tomography, *Geophys. J. Int.,* **2**(152), 280–301.

Bunge, H.-P. & Richards, M., 1996. The origin of large-scale structure in mantle convection: effects of plate motions and viscosity stratification, *Geophys. Res. Lett.,* **23,** 2987–2990.

Bunge, H.-P., Richards, M. & Baumgardner, J., 1996. The effect of depth-dependent viscosity on the planform of mantle convection, *Nature,* **379,** 436–438.

Bunge, H.-P., Richards, M. & Baumgardner, J., 1997. A sensitivity study of 3D-spherical mantle convection at 10exp8 Rayleigh number: effects of depth-dependent viscosity, heating mode and an endothermic phase change, *J. geophys. Res.,* **102,** 11 991–12 007.

Chang, S.-J., Ferreira, A. & Faccenda, M., 2016. Upper- and mid-mantle interaction between the Samoan plume and the Tonga–Kermadec slabs, *Nat. Commun.,* **7,** doi:10.1038/ncomms10799.

Chust, T.C., Steinle-Neumann, G., Dolejš, D., Schuberth, B.S.A. & Bunge, H.-P., 2017. MMA-EoS: a computational framework for mineralogical thermodynamics, *J. geophys. Res.,* **122**(12), 9881–9920.

Colli, L., Ghelichkhan, S., Bunge, H.-P. & Oeser, J., 2018. Retrodictions of Mid Paleogene mantle flow and dynamic topography in the Atlantic region from compressible high resolution adjoint mantle convection models: Sensitivity to deep mantle viscosity and tomographic input model, *Gondw. Res.,* **53,** 252–272.

Davies, D.R., Goes, S., Davies, J., Schuberth, B., Bunge, H.-P. & Ritsema, J., 2012. Reconciling dynamic and seismic models of Earth's lower mantle: the dominant role of thermal heterogeneity, *Earth Planet. Sci. Lett.,* **353–354** , 253–269.

Dubois, F., 2020, Global mantle tomography using Backus-Gilbert inversion of normal-mode and finite-frequency S-wave data. *PhD thesis,* Université de Strasbourg, Strasbourg, Grand Est, France.

Dubois, F., Lambotte, S., Zaroli, C. & Rivera, L., 2019. Global finite-frequency *S*-wave delay-times: how much crust matters, *Geophys. J. Int.,* **218**(3), 1665–1684.

Fichtner, A. & Trampert, J., 2011. Resolution analysis in full waveform inversion, *Geophys. J. Int.,* **187**(3), 1604–1624.

Fichtner, A., Zunino, A. & Gebraad, L., 2018. Hamiltonian Monte Carlo solution of tomographic inverse problems, *Geophys. J. Int.,* **216**(2), 1344–1363.

French, S.W. & Romanowicz, B., 2015. Broad plumes rooted at the base of the Earth's mantle beneath major hotspots, *Nature,* **525,** 95–9.

Gudmundsson, O., Davies, J.H. & Clayton, R.W., 1990. Stochastic analysis of global traveltime data: mantle heterogeneity and random errors in the isc data, *Geophys. J. Int.,* **102**(1), 25–43.

Horbach, A., Bunge, H.-P. & Oeser, J., 2014. The adjoint method in geodynamics: derivation from a general operator formulation and application to the initial condition problem in a high resolution mantle circulation model, *GEM - Int. J. Geomath.,* **5**(2), 163–194.

Koelemeijer, P., Ritsema, J., Deuss, A. & van Heijst, H.-J., 2015. SP12RTS: a degree-12 model of shear- and compressional-wave velocity for Earth's mantle, *Geophys. J. Int.,* **204**(2), 1024–1039.

Koelemeijer, P., Schuberth, B., Davies, D., Deuss, A. & Ritsema, J., 2018. Constraints on the presence of post-perovskite in Earth's lowermost mantle from tomographic-geodynamic model comparisons, *Earth Planet. Sci. Lett.,* **494,** 226–238.

Laske, G., Masters, G., Ma, Z. & Pasyanos, M., 2013. Update on CRUST1.0—a 1-degree Global Model of Earth's Crust, in *Geophys. Res. Abstracts,* Vol. **15,** pp. Abstract EGU2013–2658, EGU.

Maguire, R., Ritsema, J., Bonnin, M., van Keken, P.E. & Goes, S., 2018. Evaluating the resolution of deep mantle plumes in teleseismic traveltime tomography, *J. geophys. Res.,* **123**(1), 384–400.

Montelli, R., Nolet, G., Dahlen, F.A., Masters, G., Engdahl, E.R. & Hung, S.-H., 2004. Finite-frequency tomography reveals a variety of plumes in the mantle, *Science,* **303**(5656), 338–343.

Mégnin, C., Bunge, H.-P., Romanowicz, B. & Richards, M., 1997. Imaging 3-D spherical convection models: what can seismic tomography tell us about mantle dynamics?, *Geophys. Res. Lett.,* **24**(11), 1299–1302.

Müller, R.D. *et al.*, 2016. Ocean basin evolution and global-scale plate reorganization events since Pangea breakup, *Ann. Rev. Earth Planet. Sci.,* **44**(1), 107–138.

Nakagawa, T. & Tackley, P.J., 2010. Influence of initial CMB temperature and other parameters on the thermal evolution of Earth's core resulting from thermochemical spherical mantle convection, *Geochem. Geophys. Geosyst.,* **11**(6), Q06001.

Nerlich, R., Colli, L., Ghelichkhan, S., Schuberth, B. & Bunge, H.-P., 2016. Constraining central Neo-Tethys Ocean reconstructions with mantle convection models, *Geophys. Res. Lett.,* **43**(18), 9595–9603.

Nolet, G., 2008. *A Breviary of Seismic Tomography,* Cambridge Univ. Press, ISBN 978-0-521-88244-6.

Paige, C.C. & Saunders, M.A., 1982. Lsqr: an algorithm for sparse linear equations and sparse least squares, *ACM Trans. Math. Softw.,* **8**(1), 43–71.

Pijpers, F. & Thompson, M., 1992. Faster formulations of the optimally localized averages method for helioseismic inversions, *Astron. Astrophys.,* **262,** L33–L36.

Pijpers, F. & Thompson, M., 1993. The SOLA method for helioseismic inversion, *Astron. Astrophys.,* **281,** 231–240.

Rawlinson, N., Fichtner, A., Sambridge, M. & Young, M.K., 2014. Seismic tomography and the assessment of uncertainty, *Adv. Geophys.,* **55,** 1–76.

Ritsema, J., Deuss, A., van Heijst, H.J. & Woodhouse, J.H., 2011. S40RTS: a degree-40 shear-velocity model for the mantle from new Rayleigh wave dispersion, teleseismic traveltime and normal-mode splitting function measurements, *Geophys. J. Int.,* **184**(3), 1223–1236.

Ritsema, J., McNamara, A.K. & Bull, A.L., 2007. Tomographic filtering of geodynamic models: implications for model interpretation and large-scale mantle structure, *J. geophys. Res.,* **112**(B1), doi:10.1029/2006JB004566.

Sambridge, M., Bodin, T., Gallagher, K. & Tkalčić, H., 2013. Transdimensional inference in the geosciences, *Phil. Trans. R. Soc. Lond., A,* **371**(1984), 20110547.

Schaber, K., Bunge, H.-P., Schuberth, B. S.A., Malservisi, R. & Horbach, A., 2009. Stability of the rotation axis in high-resolution mantle circulation models: weak polar wander despite strong core heating, *Geochem. Geophys. Geosyst.,* **10,** Q11W04, doi:10.1029/2009GC002541.

Schuberth, B. S.A., Bunge, H.-P. & Ritsema, J., 2009a. Tomographic filtering of high-resolution mantle circulation models: can seismic heterogeneity be explained by temperature alone?, *Geochem. Geophys. Geosyst.,* **10**(5), Q05W03, doi:10.1029/2009GC002401.

Schuberth, B.S.A., Bunge, H.-P., Steinle-Neumann, G., Moder, C. & Oeser, J., 2009b. Thermal versus elastic heterogeneity in high-resolution mantle circulation models with pyrolite composition: high plume excess temperatures in the lowermost mantle, *Geochem. Geophys. Geosyst.,* **10**(1), Q01W01, doi:10.1029/2008GC002235.

Schuberth, B.S.A., Zaroli, C. & Nolet, G., 2012. Synthetic seismograms for a synthetic Earth: long-period P- and S-wave traveltime variations can be explained by temperature alone, *Geophys. J. Int.,* **188**(3), 1393–1412.

Simmons, N.A., Schuberth, B.S.A., Myers, S.C. & Knapp, D.R., 2019. Resolution and covariance of the LLNL-G3D-JPS global seismic tomography model: applications to travel time uncertainty and tomographic filtering of geodynamic models, *Geophys. J. Int.,* **217**(3), 1543–1557.

Soldati, G., Boschi, L. & Piersanti, A., 2006. Global seismic tomography and modern parallel computers, *Ann. Geophys.,* **49**(4-5), 977–986.

Stixrude, L. & Lithgow-Bertelloni, C., 2007. Influence of phase transformations on lateral heterogeneity and dynamics in Earth's mantle, *Earth Planet. Sci. Lett.,* **263,** 45–55.

Tarantola, A., 1987. *Inverse Problem Theory: Methods for Data Fitting and Parameter Estimation,* Elsevier.

Voronin, S. & Zaroli, C., 2018. Survey of computational methods for inverse problems, in *Recent Trends in Computational Science and Engineering,* InTech.

Zaroli, C., 2010, Global multiple-frequency S-wave tomography of the Earth's mantle. *PhD thesis,* Strasbourg University.

Zaroli, C., 2016. Global seismic tomography using Backus – Gilbert inversion, *Geophys. J. Int.,* **207**(2), 876–888.

Zaroli, C., 2019. Seismic tomography using parameter-free Backus – Gilbert inversion, *Geophys. J. Int.,* **218**(1), 619–630.

Zaroli, C., Koelemeijer, P. & Lambotte, S., 2017. Toward seeing the Earth's interior through unbiased tomographic lenses, *Geophys. Res. Lett.,* **44**(22), 11 399–11 408.

Zaroli, C., Lambotte, S. & Lévêque, J.-J., 2015. Joint inversion of normal-mode and finite-frequency *S*-wave data using an irregular tomographic grid, *Geophys. J. Int.,* **203**(3), 1665–1681.

SUPPORTING INFORMATION

Supplementary data are available at *GJI* online.

Figure S1. Difference between the noise-free GIP model and the tomographically filtered model (i.e. based on $\mathcal{R}_m$). As noted in the main text, both models should formally be equivalent. The difference results from two effects: (1) The reparametrization that is necessary to compute the tomographically filtered model and (2) the use of ray-theory (instead of finite-frequency theory, underlying the data sensitivity matrix G of SOLA-Z16) to compute the synthetic data that is needed to compute the GIP model.

Figure S2. Difference in crustal thickness between models CRUST1.0 and CRUST2.0 for the spherical harmonics degree $s=1$. This signal contributes (together with the shape of the tomographic grid, the way $G^{\dagger}$ acts on the input data and the source–receiver configurations of the tomographic data set) to the sharp contrast in the biased-noise GIP model close the Date Line in the depth range between 530 and 660 km in Fig. 6 of the main text.

Please note: Oxford University Press is not responsible for the content or functionality of any supporting materials supplied by the authors. Any queries (other than missing material) should be directed to the corresponding author for the paper.

APPENDIX: THE GEODYNAMIC MODEL N16-EB16

For N16-EB16, mantle circulation was modelled using the parallel finite element code TERRA (Bunge & Baumgardner 1995; Bunge *et al.* 1996, 1997; Bunge & Richards 1996), which solves the conservation equations for mass, energy and momentum at infinite Prandtl number and very small Reynolds number (no inertial forces) in a spherical shell. A numerical mesh of more than 80 million finite elements was used to achieve a high resolution, which is a prerequisite for modelling global mantle flow at earth-like conditions. Large-scale flow structures are linked to the history of surface plate motions back to 230 Ma as given by the global Earthbyte model of Müller *et al.* (2016). For the CMB, a free-slip (no shear-stress) boundary condition was applied as well as a relatively high heat-flux of 12 TW (about 35 per cent of the surface heat flow), which is achieved by setting the CMB temperature to 4200 K. Except for the plate motion history model (and a minor change in the viscosity profile), model N16-EB16 is the same as model S09-M2 from Schuberth *et al.* (2009b), which was deliberately set up such as to feature

a minimum set of assumptions; that is, it represents a simple, yet sufficiently realistic, model of the mantle general circulation while complexity is reduced to a minimum. A variety of studies have shown that such simple models of mantle flow are compatible on statistical grounds with a range of observations (e.g. tomographic images, seismic body wave traveltime residuals, the geoid as well as true polar wander estimates; Schuberth *et al.* 2009a, 2012; Schaber *et al.* 2009; Davies *et al.* 2012; Koelemeijer *et al.* 2018). The seismic heterogeneity corresponding to model N16-EB16 is obtained by post-processing its temperature field using the thermodynamic mineralogical software framework MMA-EoS (Chust *et al.* 2017) and the assumption of a pyrolite composition. MMA-EoS evaluates phase equilibria and thermodynamic properties of multicomponent systems by Gibbs energy minimization. In addition, the seismic velocities derived from the thermodynamic model were corrected for the effects of anelasticity following Stixrude & Lithgow-Bertelloni (2007). For further details on the model setup the reader is referred to Nerlich *et al.* (2016).